




Enhanced tunneling magnetoresistance and spin filtering in perovskite magnetic tunnel junctions via oxygen octahedral tilting

Hongfang Li ¹, Weijin Chen ^{2,3,4,5}, Xin Luo ^{2,3,4} and Yue Zheng^{2,3,4,*}

¹*School of Materials Science and Engineering, Chongqing Jiaotong University, Chongqing 400074, China*

²*Guangdong Provincial Key Laboratory of Magnetolectric Physics and Devices, School of Physics, Sun Yat-sen University, Guangzhou 510275, China*

³*Centre for Physical Mechanics and Biophysics, School of Physics, Sun Yat-sen University, Guangzhou 510275, China*

⁴*State Key Laboratory of Optoelectronic Materials and Technologies, School of Physics, Sun Yat-sen University, Guangzhou 510275, China*

⁵*School of Materials, Sun Yat-sen University, Shenzhen 518107, China*



(Received 2 March 2022; revised 23 May 2022; accepted 21 June 2022; published 18 July 2022)

Oxygen octahedral tilting significantly reduces the symmetry of perovskites and changes the transport properties of perovskite magnetic tunnel junctions (MTJs). We investigated SrRuO₃/CaTiO₃/SrRuO₃ MTJs by first-principles simulation and predicted an intriguing coupling between oxygen octahedral tilting and tunneling magnetoresistance. We obtained higher spin polarization at the Fermi level for the SrRuO₃ electrodes with tilted octahedra, which increases the tunneling magnetoresistance value. Transmission and complex band structure analysis shows that the majority spin tunneling current in the CaTiO₃ barrier with tilted octahedra is suppressed by wave function symmetry filtering, thus producing a negative spin filtering with an efficiency close to -100% and further enhancing the TMR effect. Both phenomena disappear in the junction without oxygen octahedral tilting, hence they have resulted from lattice distortions. The effective control of the tunneling magnetoresistance via oxygen octahedral tilting could act as a way to improve the performances of perovskite spintronic devices.

DOI: [10.1103/PhysRevB.106.035126](https://doi.org/10.1103/PhysRevB.106.035126)

I. INTRODUCTION

Magnetic tunnel junctions (MTJs) are heterostructures that consist of dielectric tunneling barriers sandwiched by ferromagnetic electrodes. A typical MTJ exhibits a sizeable change in tunneling resistance with the flip of electrode magnetization direction, known as the tunneling magnetoresistance (TMR) effect. MTJs with high TMR values are the fundamental structures of hard disk reading heads [1], magnetoresistive random access memories [2], and magnetic field detectors [3]. Therefore, the development of MTJ has focused on obtaining higher TMR values, and different materials were utilized to achieve this goal. At present, the most common electrode materials include magnetic metals [4] and alloys [5–8], while the tunneling barrier materials have gone through transition metals [4,9,10], amorphous metallic oxides [5,11–13], crystalline MgO [14–16] to low-dimensional materials such as MoS₂ [17–19], layered-BN [20–22], and graphene [23–25]. TMR values of MTJs increased significantly in this process, especially after two-dimensional (2D) materials were applied. The predicted value with 2D tunneling barriers has recently exceeded 9000% [26]. However, most works on MTJs built by low-dimensional materials have not been confirmed by experiments [27] since it is difficult to prepare high-quality 2D heterostructures. Therefore, getting higher TMR values in traditional MTJs is still practical. In this regard, the application of perovskites in MTJs has been explored. A primary

characteristic of perovskites is their complex lattice distortions. Some of them have aroused important applications. For example, the ferroelectric distortions in perovskites produce tunneling electroresistance (TER) effects and developed ferroelectric tunnel junctions [28]. This application inspired the idea of using structural distortions to design new devices. Naturally, an intriguing question comes: What role will such lattice distortions play in perovskite MTJs? Several works have thoroughly discussed this topic, such as combined TER/TMR effects [29,30] and ferroelectric induced skyrmions [31] in perovskite MTJs with ferroelectric barriers. However, the ferroelectric distortions have not been reported to improve the TMR value significantly in these works.

In this paper, we consider a more common yet less investigated lattice distortion in perovskites: the oxygen octahedral tilting (OOT), which could have a closer connection to the TMR effect. Initially, the TMR effect in the MTJ was explained with the Julliere model [32], in which the electrode spin polarization has a decisive impact on the TMR value [33,34]. In ferromagnetic perovskites such as SrRuO₃, it is reported that OOT could change the magnetization via increasing localization of Ru-*d* orbitals [35], which could increase the electrode spin polarization and further enhance the TMR effect. Later, the investigation of the TMR effect went beyond the Julliere model by taking into account the wave function symmetry-dependent spin filtering of crystalline tunneling barriers [36,37], which is closely related to the lattice symmetry of the barrier layer. OOT also has a much more significant impact on lattice symmetry than ferroelectric distortions, thus spin filtering in a perovskite-based

*zhengy35@mail.sysu.edu.cn

MTJ could also be tuned by OOT. In addition, using OOT to control the TMR effect has a significant advantage: OOT is coupled to the mechanical loads, and its tilt modes and angles can be changed by lattice strain [38–40], which can be used to achieve more sensitive mechanical controllability of TMR effect. However, these effects might also reduce the performance of MTJs, and conclusions can only be drawn by making thorough investigations. Using first-principles simulation, we demonstrate how OOT is coupled to the TMR effect in perovskite MTJs and predict an enhanced TMR effect from OOT. Our findings could provide a different perspective on the relationship between lattice symmetry and spin-dependent electron transports in MTJs.

II. COMPUTATIONAL METHODS

Ground-state calculations are performed using the QUANTUM ESPRESSO package [41]. The plane-wave energy cutoff is set to 708 eV. The exchange correlation is treated in the generalized gradient approximation with the Perdew-Burke-Ernzerhof parametrization (GGA-PBE) [42]. O-2s, O-2p, Sr-4s, Sr-5s, Sr-4p, Sr-5p, Ca-3s, Ca-4s, Ca-3p, Ca-4p, Ru-4s, Ru-5s, Ru-4p, and Ru-4d states are considered to be valence states. Integrations over the first Brillouin zone are performed on a well converged $6 \times 6 \times 6$ Monkhorst-Pack grid [43] for the $Pm\bar{3}m$ SrRuO₃ unit cell and a $4 \times 4 \times 3$ grid for the $Pnma$ SrRuO₃ unit cell. For corresponding MTJs, a $6 \times 6 \times 1$ grid and a $4 \times 4 \times 1$ grid are used separately. The atomic structures are fully relaxed until Hellmann-Feynman forces acting on each ion are less than 0.02 eV \AA^{-1} , and cell stress components are less than 0.05 GPa.

Transport and complex band calculations are also performed using the QUANTUM ESPRESSO package. Relaxed electrode layers and scattering layers are stacked in the z direction (transport direction) to form MTJs, and the electrodes are considered semi-infinite. For antiparallel spin configurations, the scattering regions are doubled in the z direction when performing self-consistent field calculations. The resulting wave functions are cut in half to match semi-infinite electrodes. In transmission coefficients calculations, a $100 \times 100 k$ mesh is used for the MTJ built by $Pm\bar{3}m$ blocks and a $70 \times 70 k$ mesh is used for the MTJ built by $Pnma$ blocks. In complex band calculations, the point groups of real bands are calculated by QUANTUM ESPRESSO. The symmetries of imaginary bands are determined by analyzing the symmetries of the real bands they connected.

III. RESULTS AND DISCUSSION

A. Ground-state properties

In the following, we use SrRuO₃/CaTiO₃/SrRuO₃ MTJs as model systems to investigate relationships between OOT and TMR effects. The reasons for choosing these materials are briefly explained below. OOT includes in-phase and out-of-phase tilts of oxygen octahedra about the a , b , and c axes of the perovskite pseudocubic cell, forming 15 different tilt systems [44]. The three most common tilt systems [45] include $a^0a^0a^0$ (Glazer's notation [46]) with $Pm\bar{3}m$ space group, $a^-a^-a^-$ with $R\bar{3}c$ space group, and $a^-a^-c^+$ with $Pnma$ space group. The octahedra in the first system are not tilted, and

the latter two have tilted octahedra about all three crystallographic axes. SrRuO₃ is a metallic perovskite with a $Pnma$ structure under 820 K [47]; it also displays ferromagnetism with magnetization around $1.1 \mu_B$ per Ru ion under 160 K [48]. The coexistence of conductivity, ferromagnetism, and OOT in SrRuO₃ makes it an ideal electrode for our simulation to reveal the coupling between TMR and OOT. Still, the low Curie temperature limits its application at room temperature. In the following simulation, we assume that SrRuO₃ is ferromagnetism, corresponding to the case below 160 K in the experiment. On the other hand, the $Pm\bar{3}m$ substrates such as SrTiO₃ suppress lattice distortions in epitaxial SrRuO₃ thin films even at low temperatures; thus, OOT in epitaxial SrRuO₃ thin films is rarely investigated. In 2011, Chang *et al.* reported a restoration to a bulklike $Pnma$ structure for epitaxial SrRuO₃ thin film on SrTiO₃ substrate when the film thickness is larger than 18 unit cells [49], which gives practical significance to the discussion of OOT in SrRuO₃ thin films. On the other hand, we chose CaTiO₃ as the tunneling barrier material since it also has a $Pnma$ structure [50] while being a dielectric and nonmagnetic perovskite. Both SrRuO₃ and CaTiO₃ have $Pnma$ structure and $a^-a^-c^+$ tilt system at room temperature. Therefore, in the following simulation, we set the $Pnma$ structure as the initial structure of the system and keep the symmetry during the relaxation. The matching of tilt systems between electrodes and tunneling barriers could produce an overall $Pnma$ structure for SrRuO₃/CaTiO₃/SrRuO₃ MTJ and significantly tune the electron transport.

Our simulated SrRuO₃/CaTiO₃/SrRuO₃ MTJs are schematically shown in Fig. 1, and their ground-state properties are calculated using the QUANTUM ESPRESSO package [41]. The building blocks (electrodes and scattering regions) are stacked in the z direction to build the MTJ; after that, the whole structure is relaxed and then divided into the left/right electrodes and the scattering region. After relaxation, the interface distances of MTJ no. 1 and no. 2 are 2.03 and 1.92 Å, respectively, with a difference of only around 0.1 Å. Therefore, the difference between the interface distances should not cause significant differences in transport properties. We assume that the thickness of all electrodes is greater than 18 unit cells; hence the influence of substrates on the electrodes can be ignored. As a result, the in-plane lattice constants of all MTJs are set to the lattice constants of bulk SrRuO₃. All ionic coordinates and the z -axis lattice constant are fully relaxed. For the cubic $Pm\bar{3}m$ SrRuO₃, the calculated lattice constant is 3.9554 Å. For the orthorhombic $Pnma$ SrRuO₃, the calculated lattice constants are $a = 5.5965$ Å, $b = 5.5853$ Å, and $c = 7.8777$ Å, which is 0.53%, 0.96%, and 0.42% higher than the experimental values under room temperature [51], respectively. The slight overestimation of lattice constants is a well-known issue of the GGA-PBE approach. The tilt system of the $Pnma$ SrRuO₃ is calculated to be $a^-a^-c^+$, which includes 7.34° in-phase tilts about the [001] axis and 7.72° out-phase tilts about the [110] and $[1\bar{1}0]$ axes of the orthorhombic cell. Our simulated MTJs are assumed to be grown on SrTiO₃ substrates, while the HF-treated SrTiO₃ prefers the TiO₂ termination [52]. Therefore, the SrRuO₃/CaTiO₃ interfaces are supposed to be RuO₂/CaO terminations to maintain the stoichiometric ratio of SrRuO₃. The upper part of Fig. 1(a) shows the relaxed structure of the MTJ built by $Pm\bar{3}m$ blocks, and the overall

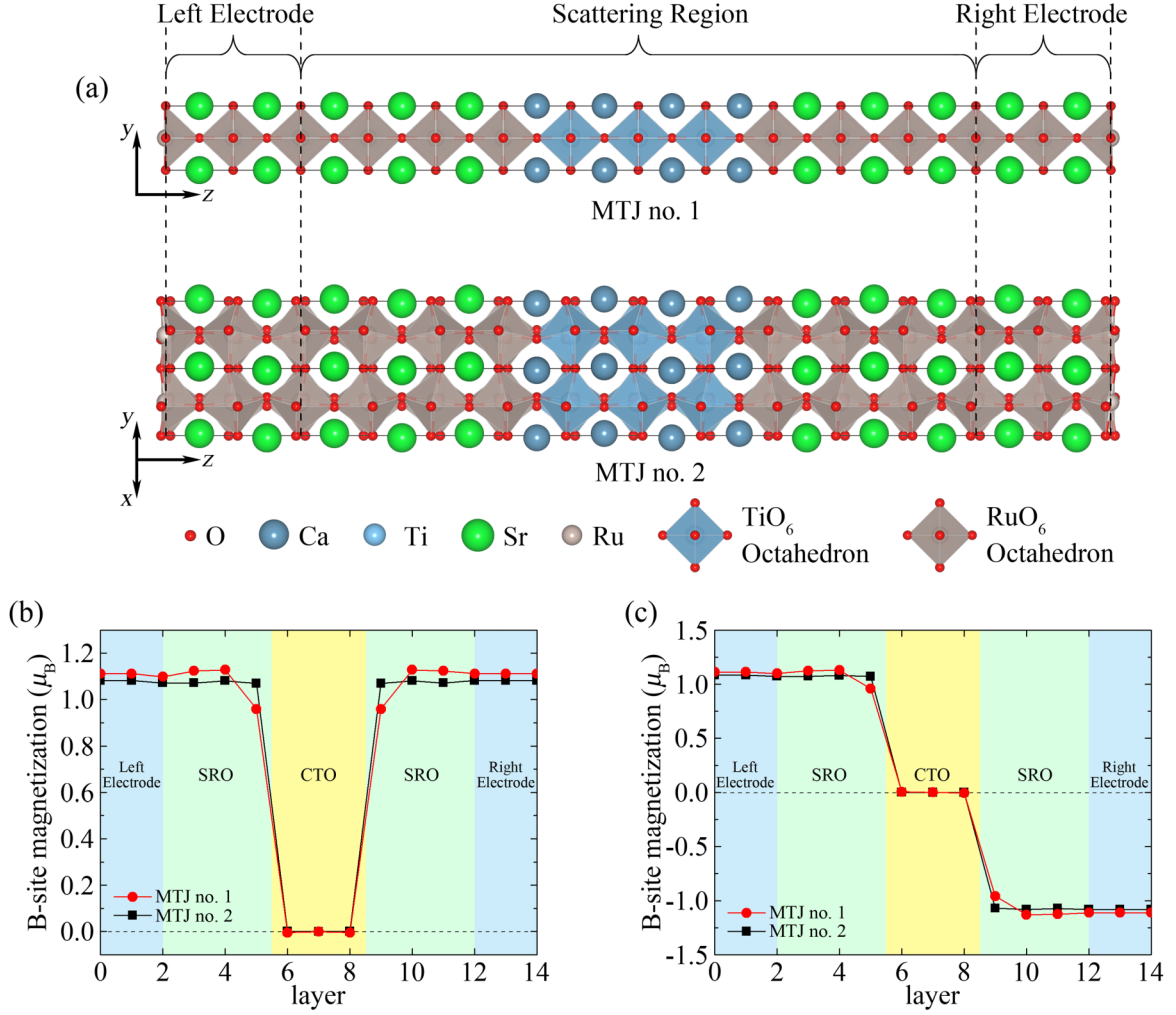


FIG. 1. (a) Schematic illustrations of MTJs in our investigation. The top is MTJ no. 1 with a tetragonal structure and $a^0a^0a^0$ tilt system (space group $P4/mmm$), and the bottom is MTJ no. 2 with an orthorhombic structure and $a^-a^-c^+$ tilt system (space group $P2_1/c$). (b) Calculated layer-averaged magnetic moments of B -site ions in MTJ no. 1 and no. 2 with spin-parallel configuration and (c) spin-antiparallel configuration.

symmetry is $P4/mmm$. The lower part of Fig. 1(a) shows the relaxed structure of the MTJ built by $Pnma$ blocks, and the overall symmetry is $P2_1/c$. The above space groups are calculated by the FINDSYM code [53]. For simplicity, we mark the $P4/mmm$ MTJ as MTJ no. 1 and the $P2_1/c$ MTJ as MTJ no. 2.

Due to our interests in the TMR effect, the most important properties of these MTJs are the ground-state magnetic moments in the SrRuO_3 layers. The corresponding calculation results are shown in Fig. 1(b). In all cases, the magnetic moments of Ru ions are about $1.1 \mu_B$, which is in good agreement with Ref. [48]. Furthermore, the magnetic moment of Ru ions in MTJ no. 1 is slightly higher than that in MTJ no. 2, but it is significantly lower than that in RuO_2/CaO interfaces. Since the SrRuO_3 layers in MTJ no. 2 maintain ferromagnetism, we expect a significant TMR effect in MTJ no. 2, which validates our following discussions.

B. Tunneling conductances of MTJ no. 1 and no. 2

The tunneling conductances of MTJ no. 1 and no. 2 under zero bias are calculated by a scattering-based approach implemented in the QUANTUM ESPRESSO package [54]. The

transmission coefficients $T(\mathbf{k}_{\parallel})$ are calculated, and all transmission coefficients (scaled by the total number and weights of k points) are summed to give the tunneling conductance for the majority (indicated by \uparrow) and the minority spin (indicated by \downarrow) channel by the Landauer formula

$$G = \frac{e^2}{h} \sum_{\mathbf{k}_{\parallel}} T(\mathbf{k}_{\parallel}), \quad (1)$$

where G is the tunneling conductance. The above formula works at 0 K, while calculating the tunneling conductance at room temperature is beyond our discussion as the temperature is assumed to be below the Curie temperature of SrRuO_3 (160 K). Therefore, we further assume that the temperature is 0 K so that Eq. (1) is applicable. We define the TMR ratio by the conventional definition

$$\text{TMR} = \frac{G_{\uparrow\uparrow} - G_{\uparrow\downarrow}}{G_{\uparrow\downarrow}}, \quad (2)$$

where $G_{\uparrow\uparrow}$ and $G_{\uparrow\downarrow}$ is the tunneling conductance of the spin parallel (indicated by $\uparrow\uparrow$) and antiparallel (indicated by $\uparrow\downarrow$) configuration, respectively. The calculated tunneling conduc-

TABLE I. Calculated tunneling conductances and TMR values for MTJ no. 1 and no. 2.

Conductance (G)	MTJ no. 1	MTJ no. 2
$G_{\uparrow\uparrow}$ (majority channel)	$3.83 \times 10^{-2} \mu\text{S}$	$1.02 \times 10^{-5} \mu\text{S}$
$G_{\uparrow\downarrow}$ (minority channel)	$3.52 \times 10^{-2} \mu\text{S}$	$2.01 \times 10^{-2} \mu\text{S}$
$G_{\uparrow\downarrow}$ (total)	$1.38 \times 10^{-2} \mu\text{S}$	$2.52 \times 10^{-5} \mu\text{S}$
TMR value	434.65%	79 807.71%

tances and TMR values for MTJ no. 1 and no. 2 are shown in Table I. Compared with MTJ no. 1, MTJ no. 2 has two distinct characteristics: the tunneling conductance decreases in both

spin-parallel and spin-antiparallel configurations, whereas the TMR value drastically increases by nearly 184 times of MTJ no. 1 (from 434.65% in MTJ no. 1 to 79 807.71% in MTJ no. 2). It is reported that the SrRuO₃ thin films grown on GdScO₃ exhibit higher resistivity than grown on SrTiO₃ due to enhanced OOT [55]; therefore, the emergence of OOT can lead to the decrease of tunneling conductivity. We believe a similar situation also appears in our systems; a reduction in tunneling conductance accompanies the OOT in MTJ no. 2. However, the mechanism for the sizeable increase in the TMR value of MTJ no. 2 is not clear.

To shed more light on the spin-dependent electron transport in MTJ no. 2, we plot the transmission coefficient $T(\mathbf{k}_{\parallel})$ at

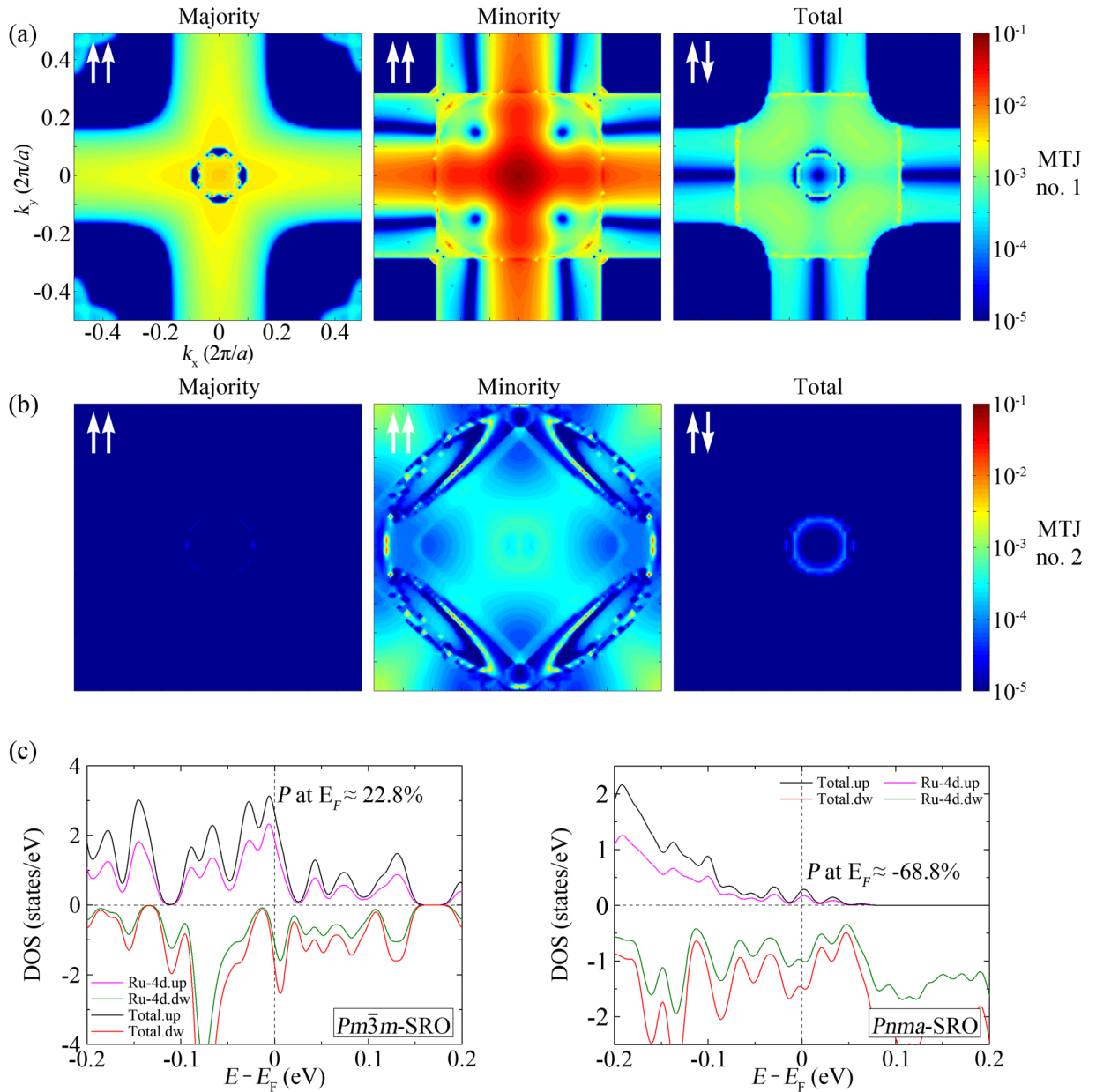


FIG. 2. (a) Calculated k_{\parallel} -resolved transmission at the Fermi level for MTJ no. 1 and (b) MTJ no. 2. White arrows show spin arrangements in left and right SrRuO₃ electrodes (i.e., spin parallel or spin antiparallel). (c) Calculated DOS in bulk SrRuO₃. The left diagram shows the DOS of $Pm\bar{3}m$ SrRuO₃, and the right diagram shows the DOS of $Pnma$ SrRuO₃. Values of spin polarization at the Fermi level (P) are given in each diagram.

each \mathbf{k}_{\parallel} point to contour maps, as shown in Fig. 2. In MTJ no. 1, it is clear that transmission near the in-plane Brillouin zone center makes a significant contribution to the tunneling conductance in the spin parallel configuration, while there is no transmission near the Brillouin zone center in the spin antiparallel configuration, as shown in Fig. 2(a). These behaviors can be explained by electrode spin polarization at the Fermi level, and symmetry mismatch between the majority and minority spin states in electrodes. In MTJ no. 2, the transmission of the majority spin channel in the spin parallel configuration is negligible, and transmissions of both majority and minority spin channels in the spin antiparallel configuration are negligible. The tunneling current can only pass through the minority spin channel in the spin parallel configuration, as shown in Fig. 2(b). These new behaviors are responsible for the remarkable significant difference between $G_{\uparrow\uparrow}$ and $G_{\uparrow\downarrow}$, hence resulting in a TMR value up to 79 807.71% in MTJ no. 2.

To further explain these phenomena, we first consider the Julliere model; the TMR effect only results from electrode spin polarization. Under this assumption, we have the Julliere formula [4]

$$\text{TMR} = \frac{2P_L P_R}{1 - P_L P_R}, \quad (3)$$

where P_L and P_R are the spin polarization of the left and right electrodes, respectively. Our simulated MTJs have symmetric electrodes and interfaces, which gives $P_L = P_R = P$. Thus the Julliere formula can be simplified as

$$\text{TMR} = \frac{2P^2}{1 - P^2}. \quad (4)$$

Under zero bias, only the states at the Fermi level contribute to the tunneling current; therefore spin polarization P used to calculate the TMR value can be expressed as [33]

$$P = \frac{D_{\uparrow}(E_F) - D_{\downarrow}(E_F)}{D_{\uparrow}(E_F) + D_{\downarrow}(E_F)}, \quad (5)$$

where $D_{\uparrow}(E_F)$ and $D_{\downarrow}(E_F)$ are the density of states at the Fermi level for the majority and minority spin channel, respectively. The magnetism of SrRuO₃ is contributed by Ru-4d orbitals, and the total density of states (DOS) and projected DOS of Ru-4d orbitals are plotted in Fig. 2(c). It is evident that although the $Pm\bar{3}m$ and the $Pnma$ SrRuO₃ have similar magnetic moments [see Fig. 1(b)], their spin polarizations at the Fermi level are quite different. The $Pnma$ SrRuO₃ has a negative spin polarization down to about -68.8%, which is nearly -3 times larger than the spin polarization in the $Pm\bar{3}m$ SrRuO₃. This result is also close to a previous theoretical predicted spin polarization of -85.7% in orthorhombic SrRuO₃ [56]. As a result, the TMR ratio of MTJ no. 2 is about 16.6 times larger than that of MTJ no. 1 from the Julliere formula, thereby partly explaining the exceptional high TMR value in MTJ no. 2. While the primary difference between the $Pm\bar{3}m$ and $Pnma$ SrRuO₃ is their lattice structure, there is no lattice distortion in the former, but complex OOT exists in the latter. Therefore, the significant increase of spin polarization in the $Pnma$ SrRuO₃ directly results from OOT, which further enhances the TMR effect in MTJ no. 2.

C. Spin-filtering effect of MTJ no. 2

It should be noted that the Julliere model can't explain the suppression of the majority spin tunneling current in MTJ no. 2 in the parallel-spin configuration [see Fig. 2(b)]. From Eq. (5), the majority spin tunneling current drops to negligible values only when $D_{\uparrow}(E_F)$ is close to zero (spin polarization decreases to about -100%). However, our calculated spin polarization of $Pnma$ SrRuO₃ is about -69%, hence the majority spin channel should still allow tunneling current in the spin parallel configuration. The above suggestion is inconsistent with Fig. 2(b). Therefore, the results in Fig. 2(b) must be explained by other mechanisms. The ability of an MTJ that only allows the current with a specific spin polarization to pass is known as the spin filtering effect [57-59], which often results from the regulation of coherent tunneling by a crystalline tunneling barrier. The spin filtering efficiency P_{sf} is defined as [60]

$$P_{sf} = \frac{I_{\uparrow} - I_{\downarrow}}{I_{\uparrow} + I_{\downarrow}}, \quad (6)$$

where the majority and minority spin components of the tunneling current are I_{\uparrow} and I_{\downarrow} . As I is linearly proportional to the tunneling conductance G under zero bias, we rewrite the above expression as

$$P_{sf} = \frac{G_{\uparrow} - G_{\downarrow}}{G_{\uparrow} + G_{\downarrow}}. \quad (7)$$

From Table I, the P_{sf} of MTJ no. 1 in the parallel-spin configuration is about 4.2%, while that in MTJ no. 2 is about -99.9%. In antiparallel-spin configurations, the P_{sf} of MTJ no. 1 and no. 2 are -2.2% and -15.8% respectively. Therefore, there is no obvious spin filtering in MTJ no. 1, but MTJ no. 2 blocks the electrons in the majority spin channel, with the largest P_{sf} going up to nearly -100%. To gain more insight into this behavior of MTJ no. 2, we plot the calculated electronic band structures along the transport direction for SrRuO₃ and CaTiO₃ in Fig. 3. The left part of Fig. 3(a) shows the real band structure near the MTJ Fermi level of $Pm\bar{3}m$ SrRuO₃; the Bloch states at the Fermi level include a majority spin state with the Δ_1 symmetry and two doubly degenerate minority spin states with the Δ_5 symmetry. The right part of Fig. 3(a) shows the complex band structure of $Pm\bar{3}m$ CaTiO₃ at $\mathbf{k}_{\parallel} = (0, 0)$ and $k_z = q + ik$. The real bands form a band gap near the Fermi level, while several imaginary bands cross the Fermi level. Each intersection of the imaginary band and the Fermi level represents an eigenchannel of tunneling. The imaginary wave vector κ indicates the decay rate of a scattering state. The scattering states at E_F in $Pm\bar{3}m$ CaTiO₃ with the lowest decay rates consist of one state with the Δ_1 symmetry and two doubly degenerate states with the Δ_5 symmetry. Since CaTiO₃ is nonmagnetic, each of its bands consists of spin-up and spin-down subbands, thus the spin and symmetry of the scattering states are perfectly consistent with the Bloch states at E_F in $Pm\bar{3}m$ SrRuO₃ electrode. On the other hand, the decay rates of the different scattering states are close, indicating that the barrier heights experienced by the majority and minority spin tunneling electrons are similar. As a result, MTJ no. 1 has no obvious preference for the majority and minority spin tunneling current. The left part of Fig. 3(b) shows the real

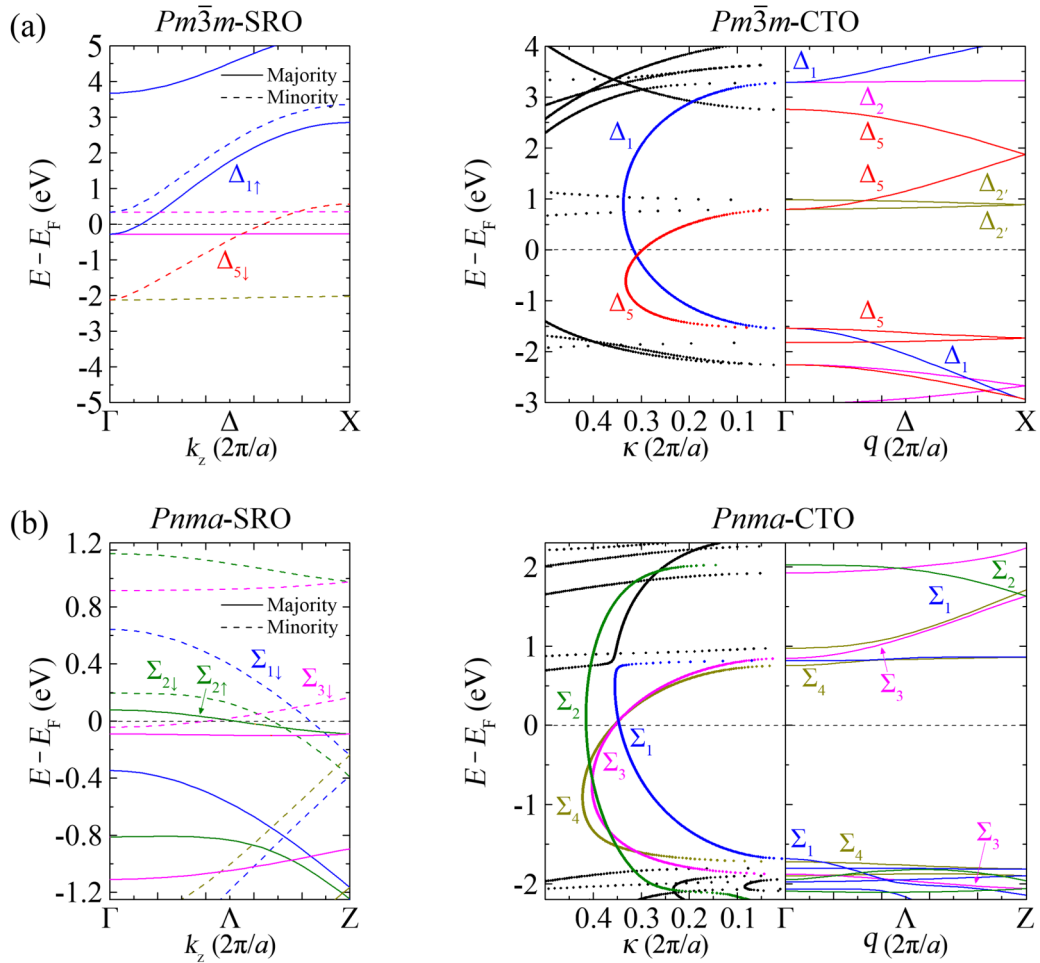


FIG. 3. Calculated complex band structures of bulk SrRuO₃ and CaTiO₃ at $k_{\parallel} = 0$. The left parts show the real bands along the transport direction near the Fermi level of SrRuO₃. The right parts show the complex bands along the transport direction near the Fermi level of CaTiO₃. The horizontal black dashed lines mark the Fermi levels. (a) Real and complex band structure of $Pm\bar{3}m$ SrRuO₃ and CaTiO₃. (b) Real and complex band structure of $Pnma$ SrRuO₃ and CaTiO₃.

band structure near the Fermi level of $Pnma$ SrRuO₃; the Bloch states at the Fermi level include a majority spin state with the Σ_2 symmetry and three minority spin states with the Σ_1 , Σ_2 , and Σ_3 symmetry, respectively. While the three scattering states at E_F in the $Pnma$ CaTiO₃ with the lowest decay rates have the Σ_1 , Σ_3 , and Σ_4 symmetry, the majority and minority spin Σ_2 scattering states have significantly larger decay rates, thus resulting in a negative spin filtering effect, as shown in the right part of Fig. 3(b). The spin filtering could effectively reduce the majority spin tunneling current in MTJ no. 2. Since MTJ no. 1 and no. 2 are identical in materials composition, their only difference is whether the oxygen octahedra are tilted or not. Therefore, we suggest that the symmetry filtering in MTJ no. 2 directly results from OOT.

Finally, we connect the symmetry of the scattering states in MTJ no. 1 and no. 2 with the atomic orbital characteristics of tunneling currents to get more insight into the negative spin filtering effect in MTJ no. 2. The calculated point group of the Δ bands in the cubic $Pm\bar{3}m$ cell of SrRuO₃ and CaTiO₃ is C_{4v} , and its irreducible representations and corresponding d -orbital wave functions are Δ_1 (d_{z^2}), Δ'_1 , Δ_2 ($d_{x^2-y^2}$), Δ'_2 (d_{xy}), and Δ_5 (d_{xz} , d_{yz}). From Fig. 3(a), it is clear that the

majority spin scattering state has the Δ_1 symmetry, hence it should include the contributions of Ru- d_{z^2} and Ti- d_{z^2} orbitals. The doubly degenerated minority spin scattering states have the Δ_5 symmetry, hence they include the contributions of Ru- d_{xz} , Ru- d_{yz} , Ti- d_{xz} , and Ti- d_{yz} orbitals. These relationships between scattering states and atomic orbitals can be verified by analyzing tunneling electrons' real space probability density distribution. Further calculations suggest that there are three eigenchannels at $\mathbf{k}_{\parallel} = (0, 0)$ of MTJ no. 1: one majority spin Δ_1 channel with the transmission $|T|^2 \approx 0.0035$, and two minority spin Δ_5 channels with identical transmissions of $|T|^2 \approx 0.0056$. The real space probability density of these scattering states of MTJ no. 1 is shown in Fig. 4; the majority spin Δ_1 state is formed by Ru- d_{z^2} and Ti- d_{z^2} orbitals, while the doubly degenerated minority spin Δ_5 states are formed by Ru- d_{xz} , Ru- d_{yz} , Ti- d_{xz} , and Ti- d_{yz} orbitals. These results closely follow our previous complex band calculation and symmetry analysis.

The next step is to apply the same method to MTJ no. 2. The calculated point group of the Λ bands in the orthorhombic $Pnma$ cell of SrRuO₃ and CaTiO₃ is C_{2v} , and its irreducible representations and corresponding d -orbital wave functions

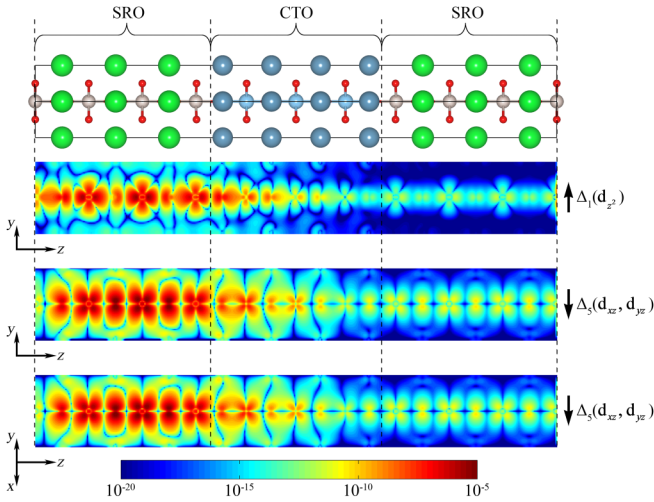


FIG. 4. Real space scattering states at the Fermi level of MTJ no. 1. From top to bottom are the majority spin scattering state with Δ_1 symmetry and two doubly degenerated minority spin scattering states with Δ_5 symmetry.

are $\Sigma_1 (d_{z^2})$, $\Sigma_2 (d_{xy})$, $\Sigma_3 (d_{xz})$, and $\Sigma_4 (d_{yz})$. Figure 3(b) shows that the majority spin Bloch state at the Fermi level in *Pnma* SrRuO₃ has Σ_2 symmetry; hence it is formed with the participation of Ru- d_{xy} orbitals. These orbitals extend perpendicular to the transport direction, so they cannot overlap with other orbitals effectively in the transport direction, therefore they should not contribute significantly to the tunneling current. Complex band calculations of *Pnma* CaTiO₃ also support this conclusion, as the three scattering states with the lowest decay rates at the Fermi level have $\Sigma_1 (d_{z^2})$, $\Sigma_3 (d_{xz})$, and $\Sigma_4 (d_{yz})$ symmetry, and all these orbitals have significant extension in the transport direction, as shown in the right part of Fig. 3(b). Eventually, the majority spin tunneling current travels from SrRuO₃ to CaTiO₃ and is suppressed due to wave function symmetry mismatch, which is further due to the majority spin Fermi surface of *Pnma* SrRuO₃, which is formed by in-plane extended Ru- d_{xy} orbitals. Transport calculations also suggest that the transmission of the Σ_2 majority spin tunneling channel at $\mathbf{k}_{\parallel} = (0, 0)$ of MTJ no. 2 is negligible, while there are two minority spin tunneling channels of MTJ no. 2 with non-negligible transmissions: one channel with $|T|^2 \approx 0.0029$, and another channel with $|T|^2 \approx 0.0020$. The real space probability density of these two scattering states in MTJ no. 2 is shown in Fig. 5, and it is evident that the upper two are Σ_2 states formed by Ru- d_{xy} and Ti- d_{xy} orbitals, and the lower two are Σ_1 states formed by Ru- d_{z^2} and Ti- d_{z^2} orbitals and Σ_3 state formed by Ru- d_{xz} and Ti- d_{xz} orbitals. These channels are also reflected in Fig. 3(b), as the minority spin Bloch states at the Fermi level of *Pnma* SrRuO₃ have $\Sigma_1 (d_{z^2})$, $\Sigma_2 (d_{xy})$, and $\Sigma_3 (d_{xz})$ symmetry, and the symmetry of the Σ_1 and Σ_3 states are consistent with the scattering states with the lowest decay rates in the tunneling barrier, which eventually form two minority spin tunneling channels with obvious transmissions. As a result, the spin filtering in MTJ no. 2 is explained by the wave function symmetry filtering of the majority spin channel. This spin filtering effect exists in both spin parallel and antiparallel configurations of MTJ

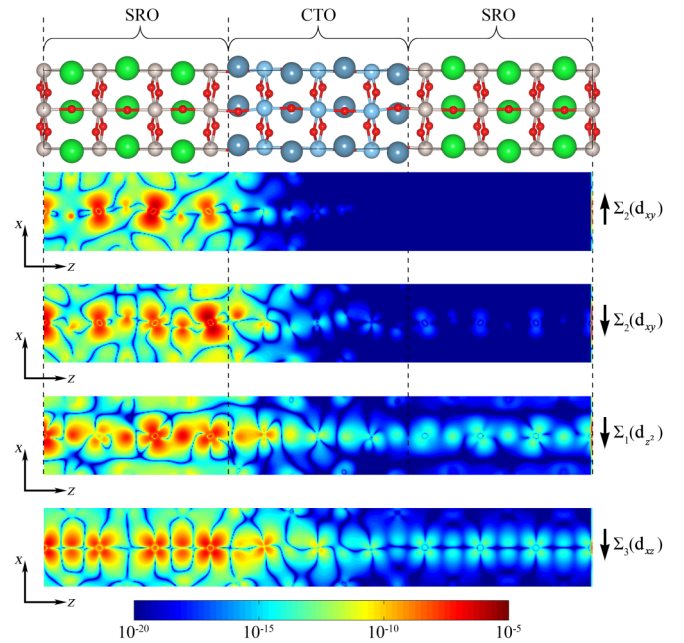


FIG. 5. Real space scattering states at the Fermi level of MTJ no. 2. From top to bottom are the majority spin scattering state with Σ_2 symmetry and three minority spin scattering states with Σ_2 , Σ_1 , and Σ_3 symmetry, respectively.

no. 2, and it further improves the TMR value of MTJ no. 2 because it drastically cuts down the already small minority carrier tunneling current in the spin antiparallel case; thus the TMR value of MTJ no. 2 eventually rises to even higher than the expectation of the Julliere model.

D. An overall picture of spin-dependent transport of MTJ no. 1 and no. 2

The above discussions provide an overall picture of spin-dependent electron transport in our simulated MTJs. Both MTJ no. 1 and no. 2 have SrRuO₃/CaTiO₃/SrRuO₃ configurations with identical electrode/barrier thicknesses and interfaces, while OOT is allowed in MTJ no. 2. We obtained sizeable oxygen octahedral tilts in MTJ no. 2, which changes the MTJ from a tetragonal *P4/mmm* structure (without oxygen octahedral tilts) to an orthorhombic *P2₁/c* structure (with oxygen octahedral tilts). Further simulations revealed that MTJ no. 2 has a much higher TMR value than MTJ no. 1, accompanied by a substantial increase in spin filtering efficiency. We showed two mechanisms for these enhancements. First, the spin polarization at the Fermi level of *Pnma* SrRuO₃ electrode in *P2₁/c* MTJ is near -12.6 times higher than that of *Pm $\bar{3}m$* SrRuO₃ in *P4/mmm* MTJ, as schematically shown in Fig. 6. The magnitudes of $D_{\uparrow}(E_F)$ and $D_{\downarrow}(E_F)$ are represented by the lengths of red and blue dashed lines. The difference between $D_{\uparrow}(E_F)$ and $D_{\downarrow}(E_F)$ in Fig. 6(b) is much more significant than in Fig. 6(a), enhancing the difference between majority carrier and minority carrier currents. At the same time, the *Pnma* CaTiO₃ tunneling barrier in *P2₁/c* MTJ produces symmetry filtering on the input current from *Pnma* SrRuO₃, which results in a negative spin filtering effect with maximum filtering efficiency of -100% . The robust spin

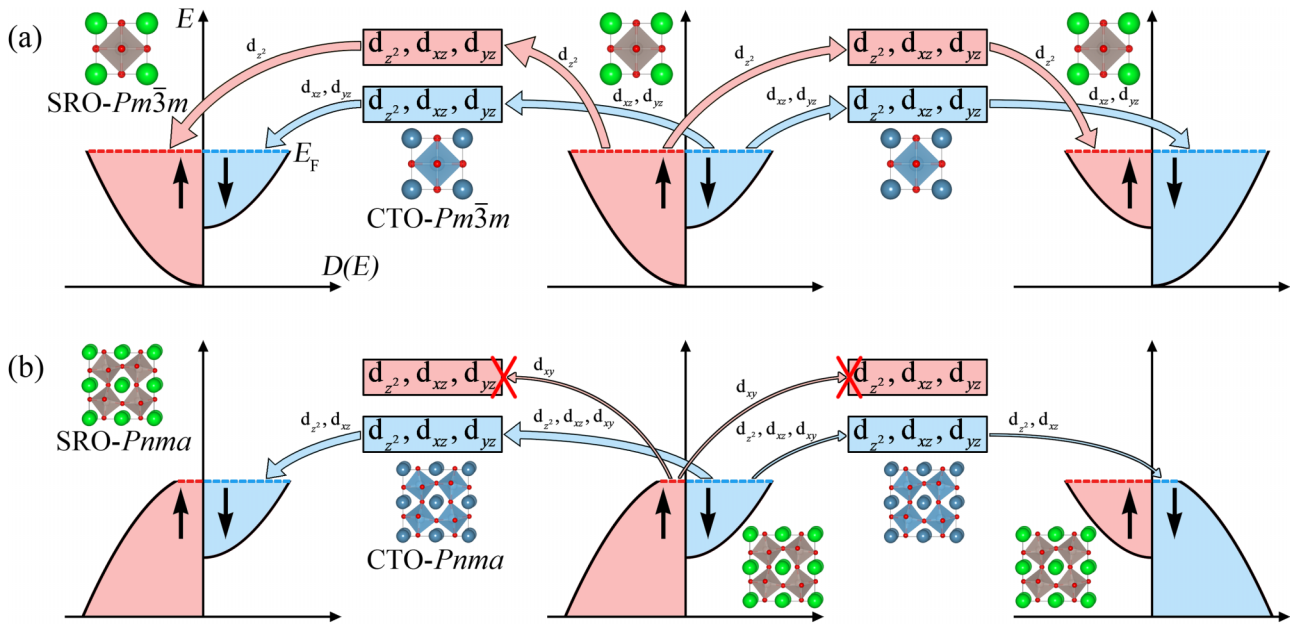


FIG. 6. Schematic illustration of spin-dependent electronic transports of (a) MTJ no. 1 and (b) MTJ no. 2.

filtering reduces the already negligible minority carrier current in MTJ no. 2, which further enhances its TMR value, as shown in Fig. 6(b). The above phenomena only occur in MTJ no. 2; we suggest they are the direct results of OOT.

IV. CONCLUSIONS

In conclusion, we use SrRuO₃/CaTiO₃/SrRuO₃ magnetic tunneling junctions as model systems to study the influences of oxygen octahedral tilting on the TMR effect in perovskite. The results show that the $a^-a^+c^-$ octahedral tilt system improves the electrode spin polarization and the spin-dependent symmetry filtering of the tunneling barrier simultaneously, resulting in a very high TMR value. This result reveals the strong coupling between oxygen octahedral tilting and spin-dependent electron transport. Due to the high degree of freedom of oxygen octahedra tilting and its strong controllability from strain and interface engineering, there are plenty of possibilities to be explored in this field. Although the Curie temperature of SrRuO₃ is too low to be applied at room temperature, we have predicted that OOT can enormously enhance the TMR effect. One can choose perovskite electrodes with high Curie temperature and tilted octahedra for practical applications of the possibly OOT-enhanced TMR effect (such

as LSMO), which will be discussed in our following works. From the perspective of applications, a higher TMR value in all-perovskite MTJs with the presence of OOT can be used to fabricate MRAM devices with better performance, and the spin filtering also lays a foundation for applications in high-performance spin detectors. We look forward to the further experimental verification of the above application potentials of oxygen octahedral tilting in all-perovskite spintronics.

ACKNOWLEDGMENTS

This work was supported by the National Natural Science Foundation of China (Grants No. 11972382, No. 12132020, and No. 12172386) and the National Natural Science Foundation of Guangdong Province, China (Grant No. 2021B1515020021). The simulations reported were performed on resources provided by the National Supercomputer Center in Guangzhou and the Rosamond Computation Center in School of Physics at Sun Yat-sen University.

Y.Z. conceived the research. H.L. designed and performed the calculation. W.C. and H.L. wrote the manuscript. All authors discussed the results and commented on the manuscript. The authors declare no competing financial interest.

- [1] K. Tsunekawa, D. D. Djayaprawira, M. Nagai, H. Maehara, S. Yamagata, and N. Watanabe, Giant tunneling magnetoresistance effect in Low-resistance CoFeB/MgO(001)/CoFeB magnetic tunnel junctions for Read-head applications, *Appl. Phys. Lett.* **87**, 072503 (2005).
- [2] S.-W. Chung, T. Kishi, J. W. Park, M. Yoshikawa, K. S. Park, T. Nagase, K. Sunouchi, H. Kanaya, G. C. Kim, K. Noma *et al.*, 4Gbit Density STT-MRAM using perpendicular MTJ

realized with compact cell structure, in *2016 IEEE International Electron Devices Meeting (IEDM)* (IEEE, San Francisco, CA, USA, 2016), p. 27.1.1–27.1.4.

- [3] Z. Jin, M. A. I. Mohd Noor Sam, M. Oogane, and Y. Ando, Serial MTJ-based TMR sensors in bridge configuration for detection of fractured steel bar in magnetic flux leakage testing, *Sensors* **21**, 668 (2021).

- [4] M. Julliere, Tunneling between ferromagnetic films, *Phys. Lett. A* **54**, 225 (1975).
- [5] H. X. Wei, Q. H. Qin, M. Ma, R. Sharif, and X. F. Hana, 80% Tunneling magnetoresistance at room temperature for thin Al–O barrier magnetic tunnel junction with CoFeB as free and reference layers, *J. Appl. Phys.* **101**, 09B501 (2007).
- [6] M. Oogane, Y. Sakuraba, J. Nakata, H. Kubota, Y. Ando, A. Sakuma, and T. Miyazaki, Large tunnel magnetoresistance in magnetic tunnel junctions using Co_2MnX ($X = \text{Al, Si}$) heusler alloys, *J. Phys. D: Appl. Phys.* **39**, 834 (2006).
- [7] T. Roy, M. Tsujikawa, and M. Shirai, IrCrMnZ ($Z = \text{Al, Ga, Si, Ge}$) heusler alloys as electrode materials for MgO-based magnetic tunneling Junctions: a first-principles study, *J. Phys. D: Appl. Phys.* **55**, 125303 (2021).
- [8] B. Pradines, L. Calmels, and R. Arras, Robustness of the Half-Metallicity at The Interfaces in Co_2MnSi -Based All-Full-Heusler-Alloy Spintronic Devices, *Phys. Rev. Appl.* **15**, 034009 (2021).
- [9] M. N. Baibich, J. M. Broto, A. Fert, F. Nguyen Van Dau, F. Petroff, P. Etienne, G. Creuzet, A. Friederich, and J. Chazelas, Giant Magnetoresistance of (001)Fe/(001)Cr Magnetic Superlattices, *Phys. Rev. Lett.* **61**, 2472 (1988).
- [10] G. Binasch, P. Grünberg, F. Saurenbach, and W. Zinn, Enhanced magnetoresistance in layered magnetic structures with antiferromagnetic interlayer exchange, *Phys. Rev. B* **39**, 4828 (1989).
- [11] T. Miyazaki and N. Tezuka, Giant magnetic tunneling effect in Fe/ Al_2O_3 /Fe junction, *J. Magn. Magn. Mater.* **139**, L231 (1995).
- [12] J. S. Moodera, L. R. Kinder, T. M. Wong, and R. Meservey, Large Magnetoresistance at Room Temperature in Ferromagnetic Thin Film Tunnel Junctions, *Phys. Rev. Lett.* **74**, 3273 (1995).
- [13] M. A. Alsaiani, N. A. Alhemiary, A. Umar, and B. E. Hayden, Growth of Amorphous, anatase and rutile phase TiO_2 thin films on Pt/ TiO_2 / SiO_2 /Si (SSTOP) substrate for resistive random access memory (ReRAM) device application, *Ceram. Int.* **46**, 16310 (2020).
- [14] S. S. P. Parkin, C. Kaiser, A. Panchula, P. M. Rice, B. Hughes, M. Samant, and S.-H. Yang, Giant tunnelling magnetoresistance at room temperature with MgO (100) tunnel barriers, *Nat. Mater.* **3**, 862 (2004).
- [15] D. D. Djayaprawira, K. Tsunekawa, M. Nagai, H. Maehara, S. Yamagata, and N. Watanabe, 230% Room-temperature magnetoresistance in CoFeB/MgO/CoFeB magnetic tunnel junctions, *Appl. Phys. Lett.* **86**, 092502 (2005).
- [16] S. Ikeda, J. Hayakawa, Y. Ashizawa, Y. M. Lee, K. Miura, H. Hasegawa, M. Tsunoda, F. Matsukura, and H. Ohno, Tunnel magnetoresistance of 604% at 300 K by suppression of ta diffusion in CoFeB/MgO/CoFeB Pseudo-spin-valves annealed at high temperature, *Appl. Phys. Lett.* **93**, 082508 (2008).
- [17] W. Rotjanapittayakul, W. Pijitrojana, T. Archer, S. Sanvito, and J. Prasongkit, Spin injection and magnetoresistance in MoS_2 -based tunnel junctions using Fe_3Si heusler alloy electrodes, *Sci. Rep.* **8**, 1 (2018).
- [18] P. Kumar, A. Kumar, and D. Kaur, Spin valve effect in sputtered FL- MoS_2 and ferromagnetic shape memory alloy based magnetic tunnel junction, *Ceram. Int.* **47**, 4587 (2021).
- [19] N. Devaraj and K. Tarafder, Large magnetoresistance in a Co/ MoS_2 /graphene/ MoS_2 /Co magnetic tunnel junction, *Phys. Rev. B* **103**, 165407 (2021).
- [20] B. Sharma, A. Mukhopadhyay, L. Banerjee, A. Sengupta, H. Rahaman, and C. K. Sarkar, Ab initio study of Mono-layer 2D insulators ($\text{X}-(\text{OH})_2$ and h-BN) and their use in MTJ memory device, *Microsyst. Technol.* **25**, 1909 (2019).
- [21] W. Qiu, J. Peng, M. Pan, Y. Hu, M. Ji, J. Hu, W. Tian, D. Chen, Q. Zhang, and P. Li, Spin-dependent resonant tunneling and magnetoresistance in Ni/graphene/h-BN/graphene/Ni van der waals heterostructures, *J. Magn. Magn. Mater.* **476**, 622 (2019).
- [22] Z. Yan, X. Jia, X. Shi, X. Dong, and X. Xu, Barrier-dependent electronic transport properties in Two-dimensional MnBi_2Te_4 -based van der waals magnetic tunnel junctions, *Appl. Phys. Lett.* **118**, 223503 (2021).
- [23] E. Cobas, A. L. Friedman, O. M. J. van't Erve, J. T. Robinson, and B. T. Jonker, Graphene as a tunnel Barrier: Graphene-based magnetic tunnel junctions, *Nano Lett.* **12**, 3000 (2012).
- [24] M. Piquemal-Banci, R. Galceran, S. M.-M. Dubois, V. Zatkó, M. Galbiati, F. Godel, M.-B. Martin, R. S. Weatherup, F. Petroff, A. Fert *et al.*, Spin filtering by proximity effects at hybridized interfaces in Spin-valves with 2D graphene barriers, *Nat. Commun.* **11**, 1 (2020).
- [25] D. Li, Large magnetoresistance and efficient spin injection in Ferromagnet/Graphene/ Fe_3GeTe_2 van der waals magnetic tunnel junctions, *J. Phys. Chem. C* **125**, 16228 (2021).
- [26] J. Yang, S. Zhang, L. Li, A. Wang, Z. Zhong, and L. Chen, Rationally designed high-performance spin filter based on two-dimensional half-metal Cr_2NO_2 , *Matter* **1**, 1304 (2019).
- [27] L. Zhang, J. Zhou, H. Li, L. Shen, and Y. P. Feng, Recent progress and challenges in magnetic tunnel junctions with 2D materials for spintronic applications, *Appl. Phys. Rev.* **8**, 021308 (2021).
- [28] M. Y. Zhuravlev, R. F. Sabirianov, and E. Y. Tsymlal, Giant Electroresistance in Ferroelectric Tunnel Junctions, *Phys. Rev. Lett.* **94**, 246802 (2005).
- [29] J. P. Velev, C. G. Duan, J. D. Burton, A. Smogunov, M. K. Niranjan, E. Tosatti, S. S. Jaswal, and E. Y. Tsymlal, Magnetic tunnel junctions with ferroelectric Barriers: prediction of four resistance states from first principles, *Nano Lett.* **9**, 427 (2009).
- [30] W. Huang, Y. Liu, Z. Luo, C. Hou, W. Zhao, Y. Yin, and X. Li, Ferroelectric domain switching dynamics and memristive behaviors in BiFeO_3 -based magnetoelectric heterojunctions, *J. Phys. D: Appl. Phys.* **51**, 234005 (2018).
- [31] L. Wang, Q. Feng, Y. Kim, R. Kim, K. H. Lee, S. D. Pollard, Y. J. Shin, H. Zhou, W. Peng, D. Lee, and W. Meng, Ferroelectrically tunable magnetic skyrmions in ultrathin oxide heterostructures, *Nat. Mater.* **17**, 1087 (2018).
- [32] J. C. Slonczewski, Conductance and exchange coupling of two ferromagnets separated by a tunneling barrier, *Phys. Rev. B* **39**, 6995 (1989).
- [33] R. J. Soulen Jr., J. M. Byers, M. S. Osofsky, B. Nadgorny, T. Ambrose, S. F. Cheng, P. R. Broussard, C. T. Tanaka, J. Nowak, J. S. Moodera, and A. Barry, Measuring the spin polarization of a metal with a superconducting point contact, *Science* **282**, 85 (1998).
- [34] D. J. Monsma and S. S. P. Parkin, Spin polarization of tunneling current from Ferromagnet/ Al_2O_3 interfaces using Copper-doped aluminum superconducting films, *Appl. Phys. Lett.* **77**, 720 (2000).

- [35] A. Grutter, F. Wong, E. Arenholz, M. Liberati, A. Vailionis, and Y. Suzuki, Enhanced magnetism in epitaxial SrRuO₃ thin films, *Appl. Phys. Lett.* **96**, 082509 (2010).
- [36] W. H. Butler, X.-G. Zhang, and T. C. Schulthess, Spin-dependent tunneling conductance of Fe|MgO|Fe sandwiches, *Phys. Rev. B* **63**, 054416 (2001).
- [37] F. Greullet, C. Tiusan, F. Montaigne, M. Hehn, D. Halley, O. Bengone, M. Bowen, and W. Weber, Evidence of a Symmetry-dependent Metallic Barrier in Fully Epitaxial MgO Based Magnetic Tunnel Junctions, *Phys. Rev. Lett.* **99**, 187202 (2007).
- [38] A. Vailionis, H. Boschker, W. Siemons, E. P. Houwman, D. H. A. Blank, G. Rijnders, and G. Koster, Misfit strain accommodation in epitaxial ABO₃ Perovskites: lattice rotations and lattice modulations, *Phys. Rev. B* **83**, 064101 (2011).
- [39] A. Herklotz and K. Dorr, Characterization of tetragonal phases of SrRuO₃ under epitaxial strain by density functional theory, *Eur. Phys. J. B* **88**, 1 (2015).
- [40] S. Masys and V. Jonauskas, The crystalline structure of tensile strained SrRuO₃: a first-principles investigation, *Cryst. Growth Des.* **18**, 3397 (2018).
- [41] P. Giannozzi, S. Baroni, N. Bonini, M. Calandra, R. Car, C. Cavazzoni, D. Ceresoli, G. L. Chiarotti, M. Cococcioni, I. Dabo, and A. Dal Corso, QUANTUM ESPRESSO: a modular and Open-source software project for quantum simulations of materials, *J. Phys.: Condens. Matter* **21**, 395502 (2009).
- [42] J. P. Perdew, K. Burke, and M. Ernzerhof, Generalized Gradient Approximation Made Simple, *Phys. Rev. Lett.* **77**, 3865 (1996).
- [43] H. J. Monkhorst and J. D. Pack, Special points for Brillouin-zone integrations, *Phys. Rev. B* **13**, 5188 (1976).
- [44] C. J. Howard and H. T. Stokes, Group-theoretical analysis of octahedral tilting in perovskites, *Acta Crystallogr. Sect. B* **54**, 782 (1998).
- [45] N. A. Benedek and C. J. Fennie, Why are there so few perovskite Ferroelectrics?, *J. Phys. Chem. C* **117**, 13339 (2013).
- [46] M. Ahtee, A. M. Glazer, and H. D. Megaw, The structures of sodium niobate between 480 and 575 °C, and their relevance to Soft-phonon modes, *Philos. Mag.* **26**, 995 ((1972)).
- [47] B. J. Kennedy and B. A. Hunter, High-temperature phases of SrRuO₃, *Phys. Rev. B* **58**, 653 (1998).
- [48] A. Kanbayasi, Magnetic properties of SrRuO₃ single crystal, *J. Phys. Soc. Jpn.* **41**, 1876 (1976).
- [49] S. H. Chang, Y. J. Chang, S. Y. Jang, D. W. Jeong, C. U. Jung, Y. J. Kim, J. S. Chung, and T. W. Noh, Thickness-dependent structural phase transition of strained SrRuO₃ ultrathin Films: the role of octahedral tilt, *Phys. Rev. B* **84**, 104101 (2011).
- [50] R. Ali and M. Yashima, Space group and crystal structure of the perovskite CaTiO₃ from 296 to 1720 K, *J. Solid State Chem.* **178**, 2867 (2005).
- [51] C. W. Jones, P. D. Battle, P. Lightfoot, and W. T. A. Harrison, The structure of SrRuO₃ by Time-of-flight neutron powder diffraction, *Acta Crystallogr. Sect. C* **45**, 365 (1989).
- [52] T. Ohnishi, K. Shibuya, M. Lippmaa, D. Kobayashi, H. Kumigashira, M. Oshima, and H. Koinuma, Preparation of thermally stable TiO₂-terminated SrTiO₃(100) substrate surfaces, *Appl. Phys. Lett.* **85**, 272 (2004).
- [53] H. T. Stokes and D. M. Hatch, FINDSYM: program for identifying the Space-group symmetry of a crystal, *J. Appl. Crystallogr.* **38**, 237 (2005).
- [54] A. Smogunov, A. Dal Corso, and E. Tosatti, Ballistic conductance of magnetic co and ni nanowires with ultrasoft pseudopotentials, *Phys. Rev. B* **70**, 045417 (2004).
- [55] R. Gao, Y. Dong, H. Xu, H. Zhou, Y. Yuan, V. Gopalan, C. Gao, D. D. Fong, Z. Chen, Z. Luo, and L. W. Martin, Interfacial octahedral rotation mismatch control of the symmetry and properties of SrRuO₃, *ACS Appl. Mater. Interfaces* **8**, 14871 (2016).
- [56] J. M. Rondinelli, N. M. Caffrey, S. Sanvito, and N. A. Spaldin, Electronic properties of bulk and thin film SrRuO₃: search for the Metal-insulator transition, *Phys. Rev. B* **78**, 155107 (2008).
- [57] J. S. Moodera, X. Hao, G. A. Gibson, and R. Meservey, Electron-spin Polarization in Tunnel Junctions in Zero Applied Field with Ferromagnetic Eus Barriers, *Phys. Rev. Lett.* **61**, 637 (1988).
- [58] T. S. Santos and J. S. Moodera, Observation of spin filtering with a ferromagnetic EuO tunnel barrier, *Phys. Rev. B* **69**, 241203(R) (2004).
- [59] M. Gajek, M. Bibes, A. Barthélémy, K. Bouzehouane, S. Fusil, M. Varela, J. Fontcuberta, and A. Fert, Spin filtering through ferromagnetic BiMnO₃ tunnel barriers, *Phys. Rev. B* **72**, 020406(R) (2005).
- [60] N. M. Caffrey, D. Fritsch, T. Archer, S. Sanvito, and C. Ederer, Spin-filtering efficiency of ferrimagnetic spinels CoFe₂O₄ and NiFe₂O₄, *Phys. Rev. B* **87**, 024419 (2013).